



HAL
open science

Study for the Design of an Eddy Current Array Probe for the Imaging of Aeronautical Fastener Holes

Vincent Thomas, Pierre-Yves Joubert, Eric Vourc'H

► **To cite this version:**

Vincent Thomas, Pierre-Yves Joubert, Eric Vourc'H. Study for the Design of an Eddy Current Array Probe for the Imaging of Aeronautical Fastener Holes. *Sensor letters*, 2009, 7 (3), pp.460-465. 10.1166/sl.2009.1073 . hal-00818184

HAL Id: hal-00818184

<https://hal.science/hal-00818184>

Submitted on 18 Jul 2013

HAL is a multi-disciplinary open access archive for the deposit and dissemination of scientific research documents, whether they are published or not. The documents may come from teaching and research institutions in France or abroad, or from public or private research centers.

L'archive ouverte pluridisciplinaire **HAL**, est destinée au dépôt et à la diffusion de documents scientifiques de niveau recherche, publiés ou non, émanant des établissements d'enseignement et de recherche français ou étrangers, des laboratoires publics ou privés.

STUDY FOR THE DESIGN OF AN EDDY CURRENT ARRAY PROBE FOR THE IMAGING OF AERONAUTICAL FASTENER HOLES

Vincent Thomas, Pierre-Yves Joubert, Eric Vourc'h

SATIE, ENS Cachan, CNRS, UniverSud, 61 Av. du Président Wilson, 94230 Cachan France

(joubert@satie.ens-cachan.fr)

Abstract:

The design of an eddy current imaging array probe dedicated to the inspection of aeronautical fastener holes is presented. The probe aims at enhancing the characterisation of defects such as surface fatigue cracks as well as at simplifying the inspection procedures (limited probe displacements). In this paper, a general probe design featuring separate inducing and sensing functions is proposed and studied thanks to 3D finite element computations. Then, a first experimental validation of the structure is given. Finally alternative pickup sensor technologies are considered. A quantitative study of the influence of both the nature of the used sensors and their arrangement as part of a multisensor array is proposed and discussed.

Keywords :

Nondestructive inspection, eddy currents, imaging probe, finite element modelling, pickup coil array, printed-circuit-board coil, micro-moulded coils, bobbin coil, defects, aeronautical fastener holes, signal to noise ratio, defect signature, spatial sampling.

1. INTRODUCTION

The nondestructive inspection (NDI) of aeronautical fastening elements is a major preoccupation in the maintenance of ageing aircrafts. Indeed, these elements undergo high mechanical constraints that may provoke the apparition of fatigue

cracks [1]. Efforts are made to detect these damages in their early stage so as to optimize the life time of the aircrafts. Among the available techniques, the eddy current (EC) method is widely used for the NDI of fastening structures such as riveted lap joints or larger fasteners, since it is easy to implement, robust and sensitive to conductivity breaks [2]. In the case of large elements such as wing fasteners, the inspection requires the removal of the fastener, so that the EC probe can be introduced inside the fastener hole. A solution sensitive enough to detect small surface or buried cracks relies on the use of rotating inner probes. Here, we propose an alternative solution based on the design of a multi-sensor imaging probe. This probe aims at enhancing the defect characterization possibilities (image inversion), as well as reducing the inspection time and avoiding the use of complex mechanical positioning systems. First, we provide with the typical characteristics of an aeronautical fastener hole and the dimensions of the defects likely to occur. Second, we propose a generic structure for a probe dedicated to such a case. Third, simulations of the interactions between the probe and the considered defects are implemented and the optimization of the multi-sensor design of the probe is proposed. Then, a first experimental validation of the probe structure is given. Finally alternative sensor technologies are considered and a quantitative study of the influence of both the nature of the used sensors and their arrangement as part of a multisensor array is proposed and discussed.

2. PROBLEM DESCRIPTION AND PROPOSED GENERIC PROBE STRUCTURE

In this study we consider a typical flawed aeronautical cylindrical fastener hole made up of an aluminium based alloy (Al 2024 T3). The considered cylinder diameter and height are 52 mm 100 mm respectively. In such an aeronautical structure, high mechanical constraints may produce fatigue cracks. These cracks are classically modelled by notches of small apertures. The shape of the defects is typically half a disc if it is located inside the cylinder, and a quarter of a disc if it appears at an end of the cylinder (Fig. 1). The typical length and aperture of these notches are in the order of 1 mm and 100 μm respectively. These are the very values considered in this study. An EC sensor requires the induction of a time varying magnetic field as well as the measurement of the magnetic signature of the inspected part. There exist systems implementing bobbin coils fulfilling both those functions [2]. Here we propose a generic structure for a multi-sensor EC probe implementing separate inducing and sensing functions. Given the cylindrical geometry of the fastener hole to be inspected, the proposed inductor is a solenoid coil wound around a magnetic core and placed into the hole (Fig. 2). In such a configuration, in the absence of a defect, the direction of the EC currents generated inside the fastener is along the θ azimuth coordinate of the cylindrical coordinate system and the resulting magnetic flux density is along the z axis. This arrangement was chosen so that the EC flow perpendicularly to the main direction (z) of the defects

(Fig. 1) in order to maximize the probe sensitivity [3]. In presence of a defect, due to the local deviation of the EC, the B_z axial component of the magnetic flux density is modified and nonzero B_r radial and B_θ azimuthal components appear in the vicinity of the defect. The B_z component induced by the EC along the z axis, is not worth exploiting since it is drowned in the magnetic flux density induced by the excitation coil. On the other hand both B_z and B_r components can be advantageously considered with defect detection in view; the choice of the best magnetic flux density component constitutes the first step of the sensor design. Suitable sensor technologies shall then be identified. The next design step deals with the arrangement of the multi-sensor matrix, which aims at performing the measurement of the magnetic signature of the whole target with minimized probe displacement. These design issues will be developed in the next section.

3. MODELLING OF THE EC/DEFECT INTERACTIONS

The generic sensor architecture being fixed, the first step in the probe design consists in quantitatively studying the B_r and B_θ components due the defect. To this aim, simulations of the interactions between the inducer and a flawed fastener hole were done using a 3D finite elements modelling considering edge flux based formulation of the considered magneto-dynamic problem. The geometry of both the fastener hole and the defect are those depicted in Fig. 1, the defect being placed in the middle of the hole ($z = 50\text{mm}$), so that edge effects due to the ends of the hole can be neglected in a first approach. Given both the dimensions of the defects and the electrical conductivity of the material, which is in the order of 17.6MSm^{-1} , taking the skin effect [2] into account leads to choose an inducing current frequency in the order of tens to hundreds of kHz. With regards to the inducing solenoid coil, it was assumed to be a double layer copper winding made up of a 1 mm diameter, and featuring an outside diameter of 48 mm. Fig. 3 provides with the cartography of the simulated B_r radial and B_θ azimuthal magnetic flux densities at a fixed radius $r = 25.8 \text{mm}$, obtained with an excitation current at 100 kHz with a 1A arbitrary chosen amplitude. As expected B_r is null in absence of a defect and exhibits a bipolar signature in the vicinity of the defect due to the deviation of the EC flow. With regards to B_θ , it is null in absence of a defect as well, whereas the defect signature is quadripolar. There are three main reasons in favour of exploiting the B_r component: it is null in absence of a defect, it is of significantly higher amplitude than B_θ and a bipolar signature is more convenient than a quadripolar one, especially when sensed by a device featuring dimensions in the same order as those of the signature.

4. INFLUENCE OF THE SENSOR ARRAY TECHNOLOGY

B_r being chosen as the most interesting component to sense, there remain several design degrees of freedom relying on both the choice of the sensor technology and on their arrangement in a multi-sensor array. Among possibilities, we chose to use pickup coils, since they are particularly easy to implement and sensitive at frequencies higher than tens of kHz. Three possible good candidate pick-up coil technologies were considered: a multilayer printed circuit board technology (PCB coils), since this technology is mature, cheap and easy to implement with array integration in view, a micro-moulded coil technology (MM coils) selected for its large scale integration ability [4], and a mini bobbin coil technology (B coils), which enables a high sensitivity to be reached. The main dimensions and characteristics of the selected pick-up coils are provided in Table 1. The choice of a particular technology is mainly a matter of compromise between sensitivity, resolution and size. Considering a given pick-up coil, the design of the probe consists in optimizing the multi-sensor array arrangement and the inducer size. The proposed design method relies on three steps. Firstly, the simulated data given by the finite elements modelling is used to calculate a reference cartography of EMF, denoted EMF_{ref} , corresponding to the mapping of the fastener hole inner surface obtained by virtually moving a pick up coil with an elementary step. This EMF calculation takes the characteristics of the sensing coils (geometry, dimensions, N_L number of layers and N_T number of turns) into account. Let p ($p=1,2,\dots,N_L$) and q ($q=1,2,\dots,N_T$) be the indexes of the layers and turns of the considered coil respectively. For the considered pick-up coil, let $\Phi_{p,q}$ be the magnetic flux through the turn of index q of the p^{th} layer. One has

$$\Phi_{p,q} = \sum_{i,j} B_{r_{pq}}(i,j) \Delta S_{ij} \quad (1)$$

where i and j denote the indexes referencing the ΔS_{ij} elementary surfaces of the turn section, and $B_{r_{pq}}(i,j)$ is the simulated radial magnetic flux density on ΔS_{ij} . The EMF sensed by the considered coil centered in a given M point, placed within the air gap between the inducer and the inner wall of the hole, is computed according to the following equation

$$EMF_{ref}(M) = j\omega \sum_{p=1}^{N_L} \sum_{q=1}^{N_T} \Phi_{p,q} \quad (2)$$

where ω is the angular frequency of the inducing current. The EMF was calculated using Eq. 1 & 2 for the 3 pick-up coils of Table 1, based on the magnetic flux density cartography relative to the configuration described above. In order to compare the influence of the coil technology on the sensor response, we chose to plot the EMF_{ref} obtained when moving along a trajectory line passing through the defect along the z axis, in the Lissajous plane presented in Figure 4. The Lissajous plots obtained for the 3 coil technologies vary in amplitude, phase and shape. Indeed, they result from the integration of the magnetic flux distribution over the volume of the coils, which varies in amplitude and phase along the r radial axis. As expected, the B coil exhibits the highest sensitivity and therefore the largest magnitude in the Lissajous plots.

4. EXPERIMENTAL FEASIBILITY

A prototype probe featuring a large inducer and a single B coil sensor was build as described in section 2 and implemented for the inspection of the fastener hole coupon featuring a quarter-disc shaped defect placed at one end of the fastener hole (Fig. 1). This configuration was chosen since it constitutes the worst case of detection, due to edge effects. The sensor was moved thanks to a 4 axis displacement robot, and the EMF was measured with reference to the inducer current using a HP4192A impedance analyser. The defect signature experimentally obtained was validated against the simulated one, after edge-effect removal and amplitude normalization (Fig. 5). The signal to noise ratio of the experimental signature was determined according to [5]:

$$SNR = 20 \cdot \log \frac{\max(|EMF|)}{\sqrt{\sigma_p^2 + \sigma_q^2}} \quad (3)$$

where $\max(|EMF|)$ is the highest value of the defect signature, and σ_p and σ_q are the standard deviations of the in-phase and the in-quadrature noises respectively, both computed over a large defect free area. The obtained SNR at 100 kHz was greater than 60 dB which validates the experimental feasibility of the designed probe structure.

5. INFLUENCE OF THE SENSOR ARRAY ARRANGEMENT

In practice, the EMF cartography provided by the pick-up array corresponds to the 2D spatial sampling of the EMF_{ref} cartography, denoted EMF_s . The sampling steps along the θ and z axes are fixed by the spacing between the sensors

constituting the array, and are denoted d_θ and d_z respectively (Fig. 6). A major drawback follows from this sampling operation. Indeed, the amplitude of the sampled defect signature is strongly dependent on the sensor coil positioning relatively to the defect signature. Indeed, considering a flat coil C (Fig. 6), the amplitude of the defect signature sampled by this pickup coil is proportional to the integral of the B_r cartography through the surface of coil C. As a consequence, the amplitude of the sampled cartography EMF_s would be maximum in case (a) and is null in case (b) (Fig. 6). Thus, considering the raw EMF_s cartography, one could conclude to the absence of a defect in case (b).

Thus, to overcome this drawback and permit the thorough characterization of the defects, it is necessary to process the raw cartography so as to dispose of an EMF cartography with high spatial resolution [6], that is as close as possible to the ideal EMF_{ref} cartography. For this purpose an interpolation of the sampled cartography may be performed. Nevertheless the accuracy of such interpolation is dependent on the sensor array configuration, i.e. dependent on the sampling steps d_θ and d_z . In the case of the imaging of the defect configuration of Fig. 1, EMF_{ref} and EMF_s obtained for $d_z = 1.25$ mm and $d_\theta = 2.8^\circ$ ($d_\theta = 1.25$ mm in curvilinear coordinate system) are presented in Fig. 7 as well as both the \hat{EMF} interpolated cartography obtained from EMF_s using a cubic interpolation and the interpolation error ε defined as

$$\varepsilon = EMF_{ref} - \hat{EMF}. \quad (4)$$

In order to quantify the difference between EMF_{ref} and \hat{EMF} a relative mean square error was defined as follows:

$$\varepsilon_{RMSE} = \frac{\sum_{n,m} \varepsilon_{n,m}^2}{\sum_{n,m} EMF_{ref}^2}. \quad (5)$$

where n and m designate the discrete positions of the sensor along the z and θ axes respectively. The ε_{RMSE} was studied as a function of the sampling step due to the array arrangement, considering each of the coil technologies. Moreover, the effect of a possible lift-off of the pickup coils was taken into consideration and modelled by an additive Gaussian complex noise added to EMF_s [7]. Fig. 8-10 represent the evolution of ε_{RMSE} as a function of the sampling step in the case of sensor arrays using MM coils, PCB coils and B coils respectively. For each considered coil technology, the sampling step necessary to keep ε_{RMSE} lower or equal to 10% is indicated by points A, B and C, in the cases of SNR = 20dB, 30dB and 60dB respectively. In each case, one can note that the required sampling step is smaller than the actual size of the pickup coils (Table 1). This feature leads to consider the overlap of adjoining sensors, either by means of array realization (physical overlapping of pickup sensors) or by array implementation (moving of the probe with displacements which are non-integer multiples of the sensor size). The minimum sampling steps and overlap

determined so as to satisfy $\varepsilon_{RMSE} \leq 10\%$ are gathered in Table 2. According to this criterion, the use of MM coils is obviously the best choice, since the overlap is limited to 7% in case of SNR = 60dB, and could be avoided for higher SNRs. On the other hand, this type of coil is quite difficult to integrate and features a low sensitivity (Table 1, Fig. 4.). To satisfy the same error criterion, the PCB coils require the largest overlap among the three coil technologies (58% in the best case of SNR = 60dB). Nevertheless, the error is limited to 30 % in the worst case (SNR = 20dB, Fig. 8) and exhibits a higher sensitivity than the MM coils. Furthermore, since these coils are multilayered, one can consider the intertwining of the layers of the adjacent coils, so as to realize a physical overlapping of the sensors with reduced difference between the provided EMFs. This configuration would avoid from moving the probe during acquisitions. Finally, B coils require a minimum sampling step of about 1 mm and an overlap of 37 % to satisfy the 10% ε_{RMSE} criterion in the case of a 60dB SNR (Table 2). Such performances could be reached thanks to a staggered row arrangement of the coils associated with adequate probe rotation along the θ axis. Since the B coils are by far the most sensitive coils, this approach appears to be promising and allows an interesting trade off between acquisition speed, interpolation error and signal to noise ratio to be achieved.

4 CONCLUSION

In this paper the authors consider the design of an eddy current imaging probe dedicated to the rapid and efficient inspection of aeronautical fastener holes. First a general structure of the probe is proposed, and the interactions of a large inducing coil with the surface defects are analyzed thanks to 3D finite element computations. Then a first experimental validation of the structure is given. Finally alternative pickup sensor technologies (PCB, micromoulded and mini-bobbin coils) are considered for the realization of the pickup sensor array. These coils were comparatively studied in terms of sensitivity, spatial sampling error and derived probe structure. Mini-bobbin coils appear to provide a good trade-off between the considered performance criteria and the practical point of view. However these coils exhibit large dimensions and do not provide ideal sampling. Thanks to appropriate eddy current image inversion, further work should focus on the ability of these coils to enable accurate defect discrimination.

ACKNOWLEDGEMENTS

The authors thank M. Dessendre and H. Trétout from Dassault Aviation for their help and support.

REFERENCES

1. J. M. Papazian, J. Nardiello, R.t P. Silberstein, G. Welsh, D. Grundy, C. Craven, L. Evans, N. Goldfine, J. E. Michaels, T. E. Michaels, Y. Li, C. Laird, *International Journal of Fatigue*, 29, (2007), pp.1668-1680
2. H.L. Libby, *Introduction to electromagnetic nondestructive test methods*, Edited by Robert Kriegger Publisher Company, New York (1979).
3. P.Y. Joubert, Y. Le Bihan, *Sensors and actuators A*, 129 (2006), pp. 10-14.
4. M. Woytasik, J.-P. Grandchamp, E. Dufour-Gergam, E. Martincic, J.-P. Gilles, S. Megherbi, V. Lavalley and V. Mathet, *Microsystem Technologies*, 12 10-11 (2006) 973-978.
5. R.P.R. Hasanzadeh, A.R. Moghaddamjoo, S.H.H. Sadeghi, A.H. Rezaie, M. Ahmadi, *NDT & E International*, 41 (2008), pp 371-381
6. A Baussard, D. Prémel and J.M. Decitre, Proc. 2002 Annual Review of Progress in Quantitative Nondestructive Evaluation (2002).
7. P.-Y. Joubert – Y. Le Bihan, *International Journal of Applied Electromagnetics and Mechanics* 19, n°1-4, pp. 647 – 651 (2004)

FIGURE CAPTIONS

Fig. 1 Geometries of an aeronautical fastener hole and of typical fatigue defects.

Fig. 2. Schematic representation of the generic probe configuration.

Fig. 3. Cartographies of the B_r axial and B_θ azimuthal components of the magnetic flux density, at the surface of the fastener hole, in the vicinity of the defect of Fig. 1 (excitation current is 100kHz, 1A).

Fig. 4. Lissajous plot of the EMF obtained at the ends of the B coil, PCB coil and MM coil for the inspection of the defect of Figure 1, along a trajectory line passing through the defect area, along the z azimuthal axis.

Fig. 5. Lissajous plot of the EMF induced at the ends of a B coil pickup sensor (continuous line for experimental and dotted line for simulated data), used for the inspection of a quarter-disc defect present at the end of the fastener hole as described in Fig. 1 (after amplitude normalization, at 100kHz).

Fig. 6: Sampling of the B_r cartography by a flat coil sensor array. (a) best case of defect signature sampling by coil C. (b), worst case of defect signature sampling by coil C. Gray pixel are null, dark pixel are negative, bright pixel are positive.

Fig. 7. EMF cartographies obtained with the B-coil sensor; reference cartography (EMF_{ref}), sampled cartography (EMF_s) is the EMF sampled by the actual sensor array, \hat{EMF} is the interpolated EMF, and ε is the interpolation error.

Fig. 8. Evolution of the relative mean square error versus sampling step ($d_\theta = d_z$, expressed in curvilinear coordinate) of the sensor array using MM-coils. SNR = 20, 30, 60dB, and f=100kHz.

Fig. 9. Evolution of the relative mean square error versus sampling step ($d_\theta = d_z$, expressed in curvilinear coordinate) of the sensor array using PCB-coils. SNR = 20, 30, 60dB, and f=100kHz.

Fig. 10. Evolution of the relative mean square error versus sampling step ($d_\theta = d_z$, expressed in curvilinear coordinate) of the sensor array using B-coils. SNR = 20, 30, 60dB, and $f=100\text{kHz}$.

TABLE CAPTIONS

Table 1. Features of the pickup coils considered for the sensor array. N_L is the number of layers, N_T is the number of turns per layer, S is the sensitivity and F_c is the cutoff frequency.

Table 2. Sensor array arrangement (sampling step and sensor overlap) necessary to maintain $\varepsilon_{RMSE} < 10\%$, for MM-coil, PCB-coil, and B-coil in case of SNR = 20dB, 30dB, 60dB.

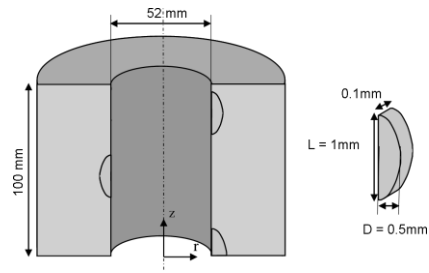


Fig. 1 Geometries of an aeronautical fastener hole and of typical fatigue defects.

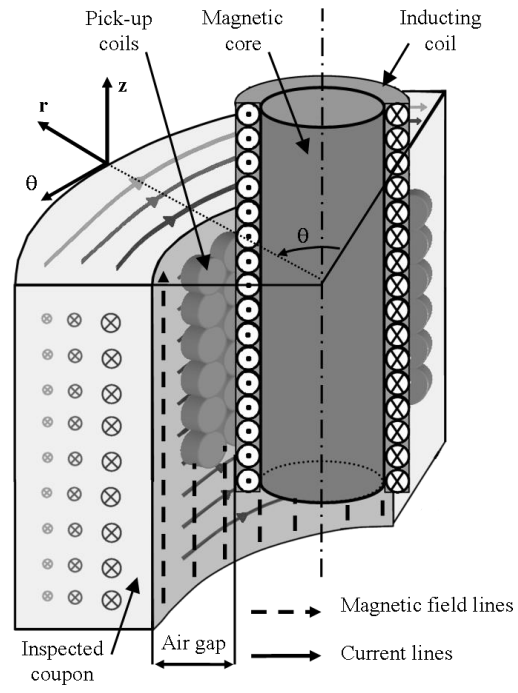


Fig. 2. Schematic representation of the generic probe configuration.

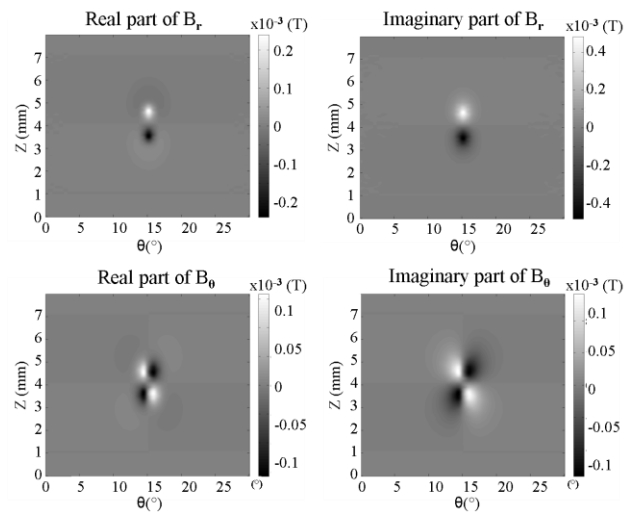


Fig. 3. Cartographies of the B_r axial and B_θ azimuthal components of the magnetic flux density, at the surface of the fastener hole, in the vicinity of the defect of Fig. 1 (excitation current is 100kHz, 1A).

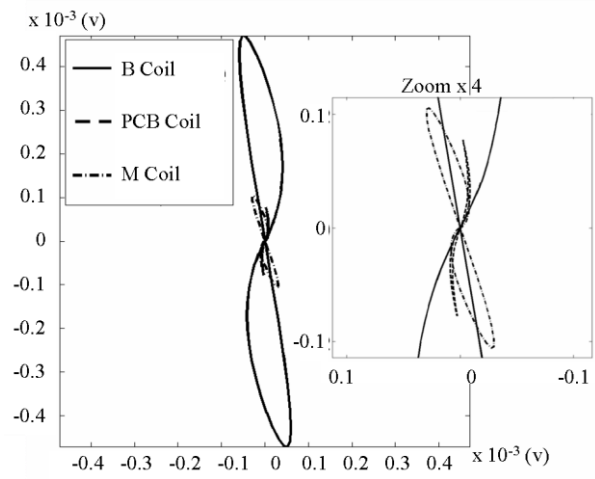


Fig. 4. Lissajous plot of the EMF obtained at the ends of the B coil, PCB coil and MM coil for the inspection of the defect of Figure 1, along a trajectory line passing through the defect area, along the z azimuthal axis.

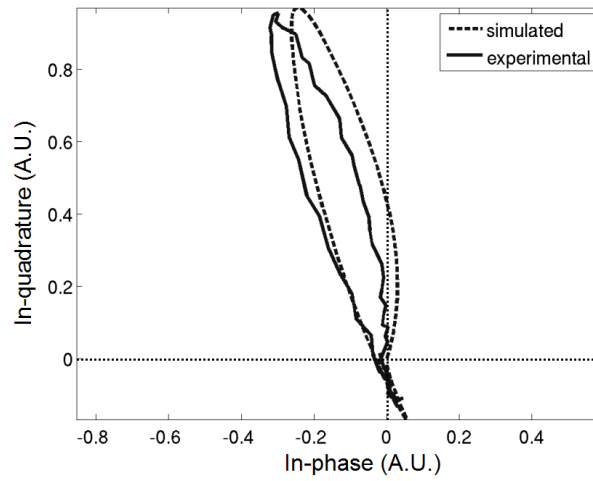


Fig. 5. Lissajous plot of the EMF induced at the ends of a B coil pickup sensor (continuous line for experimental and dotted line for simulated data), used for the inspection of a quarter-disc defect present at the end of the fastener hole as described in Fig. 1 (after amplitude normalization, at 100kHz).

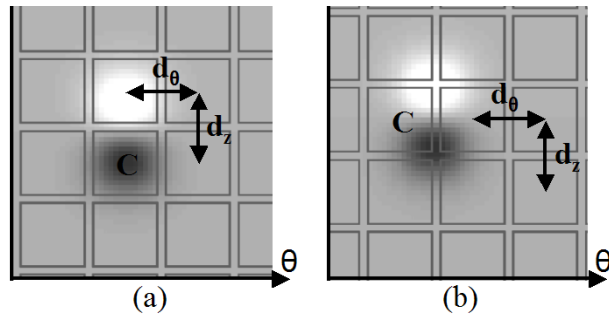


Fig. 6: Sampling of the B_r cartography by a flat coil sensor array. (a) best case of defect signature sampling by coil C. (b), worst case of defect signature sampling by coil C. Gray pixels are null, dark pixels are negative, bright pixels are positive.

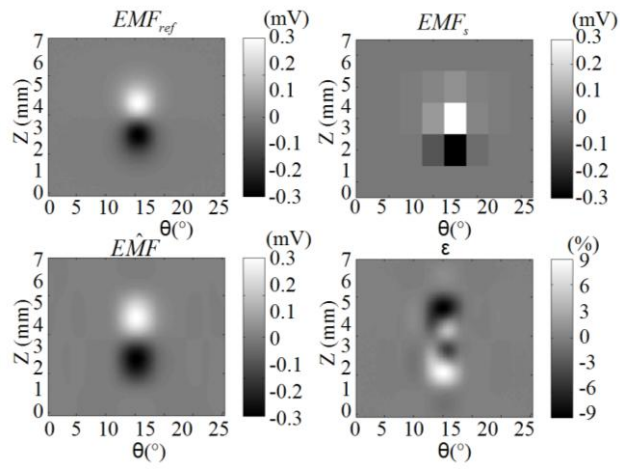


Fig. 7. EMF cartographies obtained with the B-coil sensor; reference cartography (EMF_{ref}), sampled cartography (EMF_s) is the EMF sampled by the actual sensor array, \hat{EMF} is the interpolated EMF, and ϵ is the interpolation error.

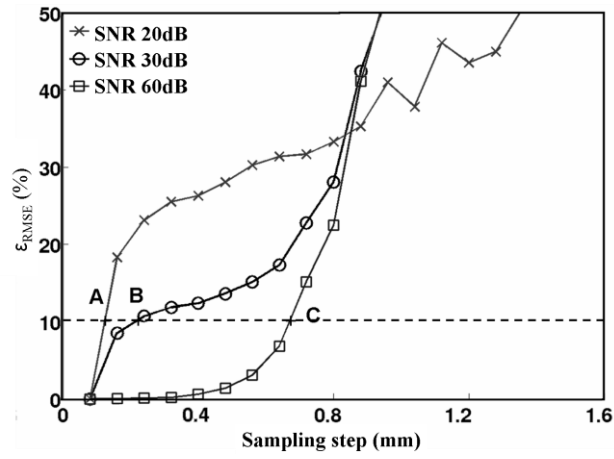


Fig. 8. Evolution of the relative mean square error versus sampling step ($d_\theta = d_z$, expressed in curvilinear coordinate) of the sensor array using MM-coils. SNR = 20, 30, 60dB, and $f=100\text{kHz}$.

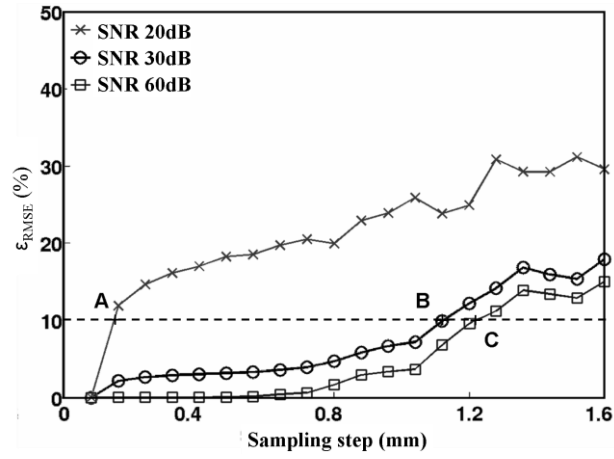


Fig. 9. Evolution of the relative mean square error versus sampling step ($d_\theta = d_z$, expressed in curvilinear coordinate) of the sensor array using PCB-coils. SNR = 20, 30, 60dB, and $f=100\text{kHz}$.

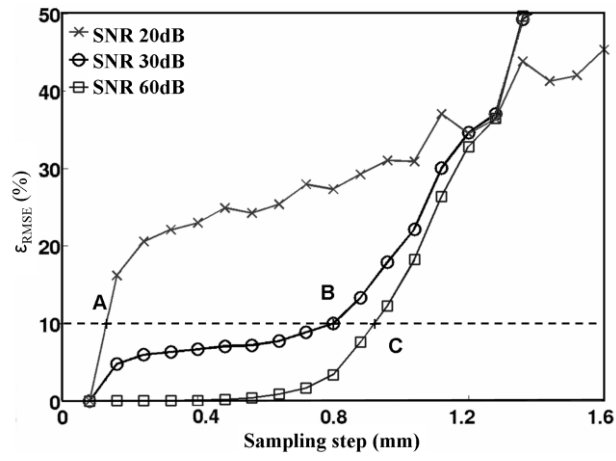


Fig. 10. Evolution of the relative mean square error versus sampling step ($d_\theta = d_z$, expressed in curvilinear coordinate) of the sensor array using B-coils. SNR = 20, 30, 60dB, and $f=100\text{kHz}$.

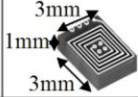
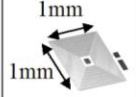
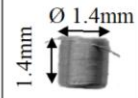
PCB Coil		$N_T = 4$ $N_L = 8$ 32 turns	$R : 3.5 \Omega$ $S : 142.5V/T@100kHz$ $F_c : >10Mhz$
MM Coil		$N_T = 40$ $N_L = 1$ 40 turns	$R : 50 \Omega$ $S : 12V/T@100kHz$ $F_c : >10Mhz$
B Coil		$N_T = 46$ $N_L = 10$ 460 turns	$R : 32 \Omega$ $S : 357.5V/T@100kHz$ $F_c : >10Mhz$

Table. 1. Features of the pickup coils considered for the sensor array. N_L is the number of layers, N_T is the number of turns per layer, S is the sensitivity and F_c is the cutoff frequency.

	Point A (SNR=20dB) Mini. sampling step (overlap)	Point B (SNR=30dB) Mini. sampling step (overlap)	Point C (SNR=60dB) Mini. sampling step (overlap)
MM Coil	0.17 mm (82.7 %)	0.29 mm (70.9 %)	0.79 mm (7.03 %)
PCB Coil	0.14 mm (95.2 %)	1.16 mm (61.3 %)	1.26 mm (58 %)
B Coil	0.13 mm (90.9 %)	0.83 mm (44.3 %)	0.94 mm (37.5 %)

Table 2. Sensor array arrangement (sampling step and sensor overlap) necessary to maintain $\epsilon_{RMSE} < 10\%$, for MM-coil, PCB-coil, and B-coil in case of SNR = 20dB, 30dB, 60dB.